JOURNAL OF SPACECRAFT AND ROCKETS
Vol. 33, No. 3, May–June 1996

Experimental and Numerical Study of Hypersonic Forward-Facing Cavity Flow

W. A. Engblom,* B. Yüceil,* D. B. Goldstein,† and D. S. Dolling‡
University of Texas at Austin, Austin, Texas 78712

Hypersonic flow over the nose of a blunt body with a forward-facing cavity is studied both experimentally (Mach 5 blowdown tunnel) and numerically (commercial finite volume code). Trends are established for the pressure oscillations within the cavity, flowfield structure, and surface heating for different cavity depths and lip radii. Resonant pressure oscillations within the cavity are an experimental flow feature but occur numerically, for the cavity geometries studied, only if freestream fluctuations are present. The oscillations are dominated by the quarter-wave frequency of the cavity. In the numerical simulations, the oscillation strength increases with cavity depth. In the experiments, oscillation strength generally increases with cavity depth; however, for a specific midrange of cavity depths, experiments show that the pressure oscillations switch randomly between two modes of behavior involving small- and large-amplitude fluctuations. Agreement between experiment and computations is good for the flowfield structure and surface heating of shallow cavity flows. Sharp lips produce both a recirculation region that cools the outer surface, and severe heating just inside the cavity. Rounding the lip eliminates the recirculation region and alleviates heating inside the cavity. Experimental results show that the strong oscillations associated with deeper cavities may produce a cooling effect.

Nomenclature

a	= speed of sound, m/s
D	= cavity diameter, cm
f	= primary frequency, Hz
G	= pressure amplification within cavity
$G(f)$	= power spectral density
L	= cavity length of depth, cm
L^*	= characteristic length, m
P_∞	= freestream static pressure, Pa
P_{base}	= basewall pressure, Pa
Pt_2	= stagnation pressure behind normal shock, Pa
s	= distance along surface, cm
T_0	= stagnation temperature, K

Introduction

HYPERVELOCITY projectiles can have large penetration depths[1,2] because of their very high kinetic energy at impact, and consequently the U.S. Army is interested in their development. However, in the flight regime of interest (2–4 km/s), the projectile nose experiences very high heating rates, and ablation can produce unacceptable perturbations in the aerodynamics and the flight path. As an example of the severity of the heating, the stagnation temperature at sea level and a velocity of about 2.8 km/s corresponds to the melting point of tungsten. There is consequently a need to develop active or passive techniques to reduce tip heating rates. There has been speculation that introducing an axial cavity in the nose region of a penetrator may reduce peak heating during flight.

Hartmann and Troll[3] introduced a technique for producing sound of high intensity and discrete frequency, known as the Hartmann whistle. This concept involves the flow of a supersonic jet over a body containing a forward-facing cavity. Research efforts related to these ideas (through the early 1960s) have been reviewed.[4] It was reported[5] more than 30 years ago that the stagnation-point heat transfer rate for a concave axisymmetric nose cone at supersonic Mach numbers is considerably lower than that of a convex nose cone. More recently, Huebner and Utreja[6] have shown that for a nose–cavity configuration the heat transfer rate at the cavity base is less than that at the rim of the nose. They also noted that the bow-shock oscillation frequency and amplitude were directly related to the cavity depth. In numerical and experimental studies,[7] good correlation between analysis and tests for the unsteady nature of the shock and the pressure distribution on the cavity wall was obtained. Marquart et al.[8] focused on the dynamics of the detached bow shock and acoustic resonance in a forward-facing nose cavity of a blunt-faced model. They found that the primary mode of pressure oscillation in the cavity is at the classical organ-pipe frequency, and that the rms levels of the fluctuating pressure along the cavity wall increased toward the base. Huebner and Utreja[9] presented a detailed description of the bow-shock behavior associated with a conical-walled cavity with a flat circular base at $M_\infty = 10$. A violent bow-shock instability occurred for one set of conditions during the test, although the primary behavior was a stable, periodically oscillating bow shock. All of these tests were conducted in facilities that produce a significant amount of freestream noise due to turbulent nozzle flow.

Preliminary experiments[10] at Mach 5 using an infrared (IR) camera carried out by two of the current authors indicated that larger-diameter, shallow cavities (length-to-diameter ratio L/D between 0.15 and 0.35) created a stable cool ring in the vicinity of the sharp cavity lip with temperatures locally lower than those of a simple spherical nose. Pressure measurements made at the center of the cavity base showed that oscillations inside the cavity had dominant frequencies close to classical organ-pipe values. The objective of the current study is to understand the fluid dynamics of hypersonic flow about a forward-facing cavity and to determine how surface heating rates and flowfield structure are affected by the presence of the cavity.

Methodology

This paper presents results from a joint experimental and computational effort to understand the fluid mechanics of such cavity flows. Approximately the same body configurations and freestream conditions were used in both the experiments and numerical simulations, to provide a direct comparison of results. The baseline case for both experiments and computations is a hemisphere–cylinder body without a cavity (i.e., $L/D = 0$).

Received March 7, 1995; revision received Sept. 6, 1995; accepted for publication Sept. 15, 1995.

*Graduate Research Assistant, Center for Aeromechanics Research, Department of Aerospace and Engineering Mechanics. Student Member AIAA.

†Assistant Professor, Center for Aeromechanics Research, Department of Aerospace and Engineering Mechanics. Member AIAA.

‡Professor, Center for Aeromechanics Research, Department of Aerospace and Engineering Mechanics. Associate Fellow AIAA.

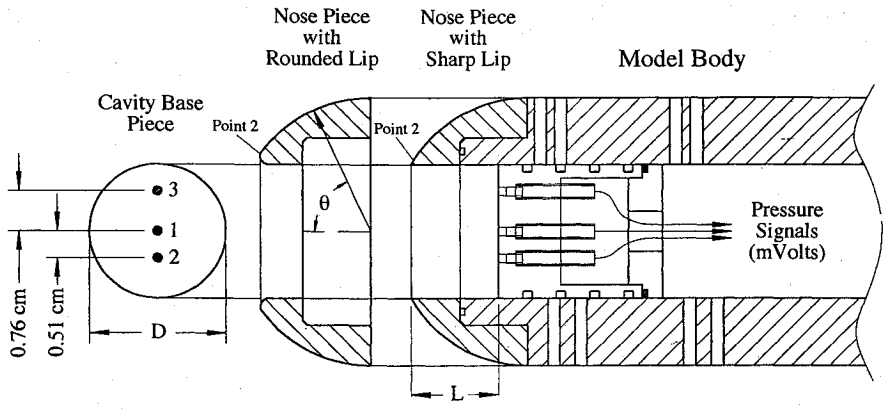

Fig. 1 Modular model design.

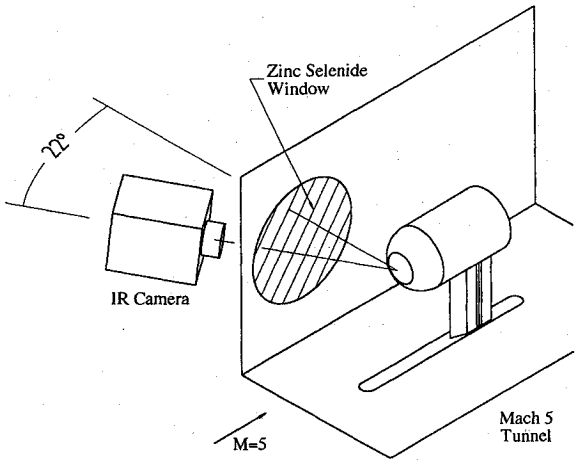

Fig. 2 Experimental setup.

Experimental Arrangement

All experimental work was conducted in the Mach 5 blowdown wind tunnel at Pickle Research Center. The tunnel was operated at a stagnation pressure and temperature of 2.275 MPa and 370–375 K, respectively, corresponding to a freestream Reynolds number of 5.0×10^7/m.

The model is a hemispherically blunted cylinder, 5.08 cm in diameter, with a variable-length cavity at the tip (Fig. 1). The cavity diameter is 2.54 cm for all cases. To explore the effects of cavity lip and base geometry, a modular model concept has been adopted (see Fig. 1). Two nose pieces, one with a sharp cavity lip and the other with ≈1.5-mm lip radius, can be screwed into the model body to form the sphere–cylinder model. Cavities are designated shallow, medium, and deep: the term shallow is used if L/D is less than 0.40, medium if L/D is between 0.40 and 0.70, and deep if L/D is greater than 0.7. By changing the axial position of the cavity insert, values of L/D ranging from 0 to 2.25 for temperature measurements and 0 to 1.5 for pressure measurements can be obtained. The L/D range is reduced for pressure measurements because of the need to accommodate pressure transducers.

Surface temperature measurements are performed using a thermal imaging system.[10] The technique is nonintrusive and is capable of acquiring a large volume of data with little effort. Despite the restrictions on the materials that can be used for the model body and the need for calibration, the system is substantially easier and quicker to construct than a model instrumented with thermocouples and related circuitry. To obtain accurate temperature measurements, polycarbonate (that has good structural properties and a very low thermal conductivity) was selected as the material for the nose pieces.

The model is installed on the centerline of the test section using a streamlined support attached to the tunnel floor (see Fig. 2). Since the camera's lens is placed at 68 deg to the freestream direction, the cavity is seen as a vertical ellipse by the camera. Table 1 shows the cavity geometries used in the IR camera experiments. The temperature histories at specific points along the outer surface are compared with results for the same surface locations on the baseline (no cavity) case.

Figure 1 also shows the insert instrumented with three transducers on the cavity base for fluctuating-pressure measurements (channels 1, 2, and 3). Kulite pressure transducers with an effective frequency response up to approximately 50 kHz and with a pressure range of 0–0.33 MPa were used. Details of the data acquisition system can be found in Ref. 11. Most of the cases were run at sampling rates of 1 MHz or 200 kHz per channel. Table 2 shows cavity geometries used in the fluctuating pressure measurements.

The cavity geometries listed in Tables 1 and 2 demonstrate experimental behavior that is characteristic of each L/D category. Rather than provide the results for all cavity geometries studied, we provide the results for one characteristic case in each category. The medium-range L/D geometries, however, demonstrate sensitivity to small geometry changes and do not contain a characteristic case. The models used in the experiments had either a spherical base shape or a flat base shape, but all numerical simulations assumed a flat base shape. This difference is not considered significant, since the behavior of the cavities in the experiments demonstrated little sensitivity to base shape, except possibly in the medium range of cavity L/D.[11] To visualize the surface shear-stress pattern in the vicinity of the cavity edge, the kerosene-lampblack technique was used. This technique indicates separation or reattachment lines on a surface as regions of tracer material accumulation or divergence.

Experimental Procedure

To avoid the effects of changing tunnel conditions, the model nose is shielded during tunnel startup with a rubber cap. The IR camera is operated continuously during the entire run. By matching the clocks on the camera and on the data acquisition system, the time when the cap is removed can be determined within 0.0167 s. The data prior to this moment are discarded. More information about the experimental procedure as well as the details of the calibration and the analysis of both temperature and pressure data can also be found in Ref. 11.

Finite Volume Code Description

A brief examination was made of several available computer codes capable of handling hypersonic flows. INCA,[12] a commercial code, was selected for this study on the basis of available documentation, technical support, and the ability to predict peak heating for the baseline case. INCA is a finite volume code that utilizes flux splitting[13] with upwinding to capture strong shocks. INCA contains an efficient LU-SGS (lower–upper successive Gauss–Seidel) implicit solver to calculate steady flowfields. The LU-SGS algorithm approximately solves the system of equations using two sweeps of a point Gauss–Seidel relaxation. An Euler step (first-order time-accurate) explicit solver is also available. All grid generation is performed using codes capable of producing orthogonal grids.

Numerical Assumptions

Several simplifying assumptions are made in the simulations. The flow is axisymmetric. In view of the small scale of the flowfield (i.e., the nose region), we assumed laminar flow. The freestream Reynolds number is roughly 5.0×10^7/m. The actual Reynolds number (per meter) is much smaller along the body surface inside the cavity and outside the cavity near the lip, because of the low-speed flow. Since

Table 1 Cavity geometries used in IR camera experiments

Cavity	L/D		
Lip	Shallow	Medium	Deep
Sharp	0.235	0.59	1.19[a]
Rounded	0.18	0.525	1.13[a]

[a]Spherical cavity base shape.

Table 2 Cavity geometries used in pressure measurements

Cavity	L/D		
Lip	Shallow	Medium	Deep
Sharp	0.23	0.57[a]	1.235
Rounded	0.17	0.51[a]	1.175

[a]Spherical cavity base shape.

Table 3 Stagnation-point heat-flux estimates for baseline case, obtained during grid refinement study, for four surface cell thicknesses t

Grid size		Heat flux, kW/m^2			
Azi.	Rad.	$t = 2.5E{-}2$	$1.0E{-}2$	$2.5E{-}3$	$2.5E{-}4$ mm
25	40	——	——	33.2	70.0
25	80	28.7	45.8	56.5	56.4
50	80	33.5	49.4	56.3	56.2
50	120	32.8	48.7	56.2	56.2

the characteristic flow lengths are less than 1 cm and a favorable pressure gradient is present, we do not expect transition to occur within regions of interest unless the oscillations within the cavity cause of flow the trip. The wall temperature is assumed isothermal ($T_{wall} = 300$ K). The temperature potential—the difference between the wall temperature and stagnation temperature—is only 71 K ($T_{stag} = 371$ K). The minimum and maximum flow temperatures in the simulations presented herein always remain at 64 K (freestream) and 500 K. Since the specific heats change less than 5.0% over this temperature range, the flow is assumed calorically perfect.

Numerical Procedure

Steady-flowfield results are obtained via the implicit LU-SGS algorithm. The pressure-field solution is obtained with a relatively coarse grid along the body surface (between 10^{-1}- and 10^{-2}-mm surface cell thickness). Spatially converged heat-flux estimates (i.e., temperature-field solutions) are obtained with a relatively fine grid near the body surface (typically between 10^{-3}- and 10^{-4}-mm surface cell thickness.

Time-accurate simulations of pressure oscillations within the cavity are conducted using the steady-flowfield solution as an initial condition followed by explicit time stepping. Since the explicit algorithm is only first-order accurate, the time step is set to one-half the allowable global value base on Courant–Friedrichs–Lewy constraints. The sensitivity of pressure oscillations to smaller time steps is negligible. Time-accurate simulation of heat-flux variations has not yet been conducted on account of the severe limitations on the allowable time step imposed by fine grids.

Code Verification

Code verification is conducted via numerical study of the baseline case. The body dimensions and the freestream conditions are the same for both the experiment and numerical simulations. Present experimental results include only a qualitative estimate of the heat-flux distribution because of changes in surface temperature and cannot provide a direct comparison with numerical heat-flux results. Hence, detailed verification involves comparison of numerical estimates for stagnation pressure and peak heat flux with other experimental and analytical values. Excellent agreement is obtained for the numerical estimate of stagnation pressure with normal shock theory (within 1%). Experimental measurement of the mean stagnation pressure varies slightly from one run to the next because of wind-tunnel tolerances but remains within 5% of the numerical prediction.

The computational result for the peak heat flux is within 7% of the analytical value estimated using a correlation developed by Fay and Riddell in 1958.[14] Their correlation was derived from extensive computations of the compressible boundary-layer similarity equations, assuming Sutherland's viscosity law, chemical equilibrium, a Newtonian pressure distribution, and a large driving temperature potential. The small driving potential for the baseline case (i.e., 71 K) may account for some disagreement with Fay and Riddell's estimate (52.2 kW/m^2).

A grid refinement study is an essential part of any code verification process. Table 3 summarizes the peak heat-flux estimates for all candidate mesh sizes. A fine grid is needed near the body surface in the radial direction (i.e., small surface cell thickness) to resolve the normal temperature gradient. A moderately fine grid is also needed to resolve the bow shock. We conclude that a surface cell thickness of 10^{-3} mm or smaller and 80 radial cells is probably sufficient for shapes similar to the baseline case.

Results

Characteristics of Resonance

Primary frequencies for different cavities can be calculated from a simple linear relation derived from the one-dimensional wave equation in classical organ-pipe theory by considering only the characteristic length and the speed of sound inside the cavity:

$$f = a/4L^* \tag{1}$$

Numerical steady-flowfield solutions indicate that the flow is virtually stagnant inside the cavity. Consequently, the speed of sound can be estimated by assuming the gas temperature inside the cavity is approximately the stagnation temperature of the flow. Hence,

$$f = \frac{\sqrt{\gamma RT_0}}{4L^*} \tag{2}$$

Time-accurate flowfield animations indicate that pressure waves travel between the bow shock and the base of the cavity. Consequently, an appropriate characteristic length is the distance between the mean bow-shock location and the cavity base along the centerline. Figure 3 shows the predictions of Eq. (2) for primary frequency vs cavity L/D. Note that Eq. (2) provides good agreement with values derived from experimental runs and time-accurate numerical simulations.

Oscillating pressure levels within a cavity are a dominant experimental flow feature in all of the cavity configurations. Resonant frequencies are obtained by spectral analysis of the fluctuating-pressure measurements made at the base of the cavity. Most of the energy of the oscillations is contained in the primary mode, which is at the lowest resonant frequency and is consequently considered as the distinctive resonant frequency of a given cavity configuration. Figure 4 contains a sample pressure–time history and corresponding power spectrum for $L/D = 0.25$ (sharp lip and flat base shape). Here var is the square of the standard deviation. The primary mode is estimated at 7000 Hz from Eq. (2), and the power-spectrum peak is approximately 6250 Hz.

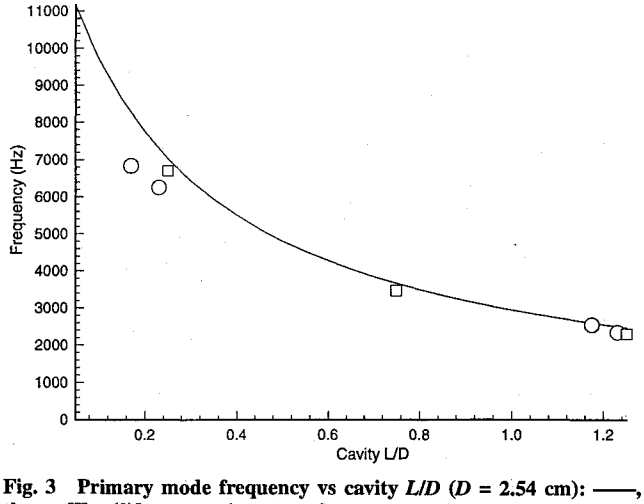

Fig. 3 Primary mode frequency vs cavity L/D (D = 2.54 cm): ——, theory [Eq. (2)]; ○, experiment; and □, computation.

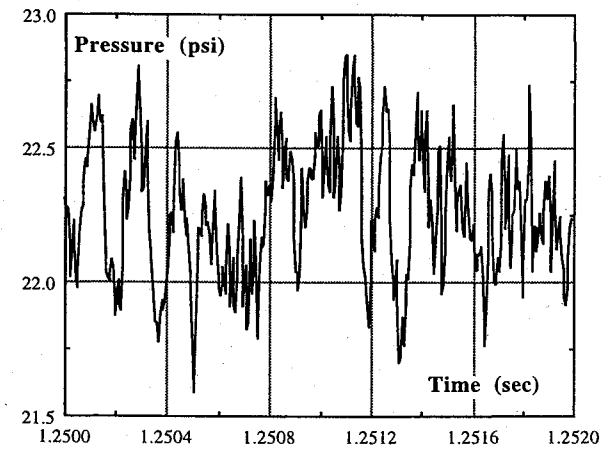

Fig. 4a Base pressure history for L/D = 0.23 (experimental).

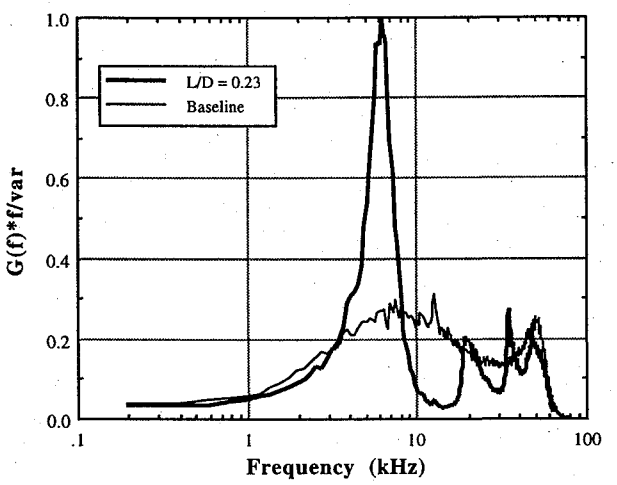

Fig. 4b Power spectrum for L/D = 0.23 (experimental).

Time-accurate numerical simulations indicate that, for truly steady freestream conditions and the modest cavity depths described here ($L/D \leq 1.25$), these oscillations rapidly dissipate until a steady flow is achieved. However, numerical resonance is obtained by introducing broad-bandwidth freestream noise (e.g., unsteady freestream pressure at the inflow boundary). The freestream pressure noise is estimated by rescaling our experimental measurements of the stagnation pressure for the baseline shape. Time-accurate results for the pressure history at the base of the cavity are presented in Fig. 5 for $L/D = 0.75$ (sharp lip and flat base shape) and estimated primary mode of 3600 Hz from Eq. (2). The freestream noise input is also shown. These pressure histories have been normalized to indicate the percentage variation from the mean value. Note that the input pressure varies by approximately ±2%. A detailed power spectrum of the simulation is difficult to obtain because of limited computer resources. However, it is clear that most of the energy of the oscillations is contained in a primary mode of approximately 3300 Hz.

Numerical resonance is also simulated by input of a sinusoidal freestream pressure. In these simulations a sinusoidal freestream inflow pressure perturbation, with a peak-to-peak amplitude of $\pm 0.02 P_\infty$, drives the pressure oscillations within the cavity at a constant frequency. This input wave results in large, nearly sinusoidal stagnation pressure oscillations at the base of the cavity. The amplification is the ratio of the output (centerline base pressure) amplitude to the input (freestream) amplitude:

$$G = \frac{|P_{\text{base max}} - \bar{P}_{\text{base}}|}{|P_{\infty \text{ max}} - \bar{P}_\infty|} \tag{3}$$

For example, a sharp-lip cavity of $L/D = 0.75$, driven with a perturbation input of $\pm 0.02 P_\infty$ at 3600 Hz, produces a perturbation output of $\pm 0.20 P_{\text{base}}$ at 3600 Hz at the cavity base, for an amplification of 10. Preliminary results indicate a strong dependance of the amplification on input frequency, especially for deep cavities. Hence, strong

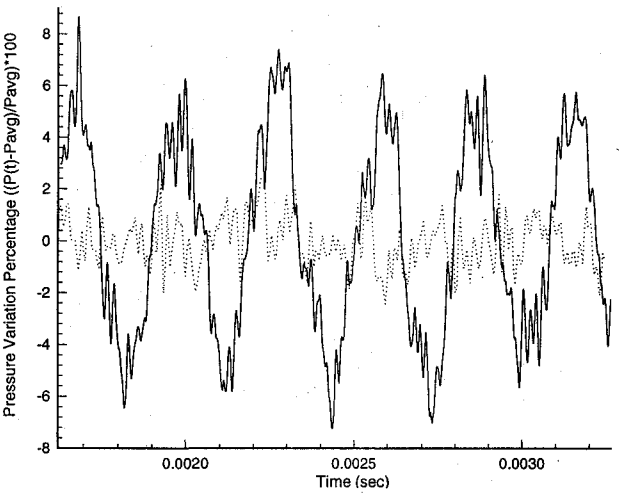

Fig. 5 Normalized base pressure history for L/D = 0.75 (numerical; freestream noise input included): ——, basewell pressure and ····, freestream pressure (noise).

numerical resonance is achieved provided the freestream noise contains energy in the primary mode. We found no numerical evidence for an alternative self-sustaining mechanism of resonance for the cavity geometries studied ($L/D \leq 1.25$). It appears that the presence of broad-bandwidth freestream turbulence in the blowdown tunnel causes the cavity to resonate.

Pressure Oscillations vs Cavity Depth

For shallow or deep cavities there is agreement between experiment and computations about the general nature of the pressure oscillations. The oscillation strength increases with cavity depth. Also, the pressure signals become cleaner (more sinusoidal)—i.e., energy is more concentrated at resonance frequencies—for deeper cavities. These trends, however, do not apply to the experiments involving medium-depth cavities.

Figure 6 shows sample experimental pressure signals measured at the center of the cavity base for shallow, medium, and deep cavity configurations. Shallow-cavity ($L/D = 0.25$) pressure signals are qualitatively similar to the baseline case, with small rms values (on the order of $1.15\% P_{t_2}$), although their power spectra reveal resonant frequencies in which the energy is concentrated unlike the baseline spectrum, which is broadband. Further, essentially all data records look alike, indicative of one mode of oscillation.

In contrast, medium-cavity ($L/D = 0.6$) pressure signals are characterized by random switching between two modes, which have different amplitudes but similar frequencies. This switching occurs many times, apparently at random intervals, during the 2.5-s duration of the run. We often find that the signals from all three locations (channels 1, 2, and 3) on the base have similar behavior, but certain characteristics of the transition to high-amplitude oscillations are worth noting. The high-amplitude mode starts with decreasing pressure levels on channel 1 and increasing levels on channel 3. Pressure levels on channel 2 usually stay between those of channels 1 and 3. This imbalance of the pressure field might be a triggering mechanism for high-amplitude oscillations. This imbalance is clearly a symptom of a nonaxial oscillation mode, perhaps involving radial, or slosh, modes. Before returning to the low-amplitude mode, all three channels experience similar oscillations, which might indicate that the pressure wave inside the cavity becomes one-dimensional towards the end of the high-amplitude mode. During the low-amplitude oscillation mode, the rms of the fluctuations is slightly larger than for shallow cavities (and is thought to characterize the simple axial mode), whereas the high-amplitude oscillations have rms values that are a large fraction (typically 50%) of the mean pressure value. This type of oscillation makes the results of standard statistical analysis difficult to interpret in that the overall rms does not truly reflect either condition. It is probable that the flow asymmetry in the medium cavity is caused by switching between axial and other oscillation modes. The reason for the switch from one oscillation mode to the other is not yet understood, but further studies are being planned to investigate this phenomenon in detail.

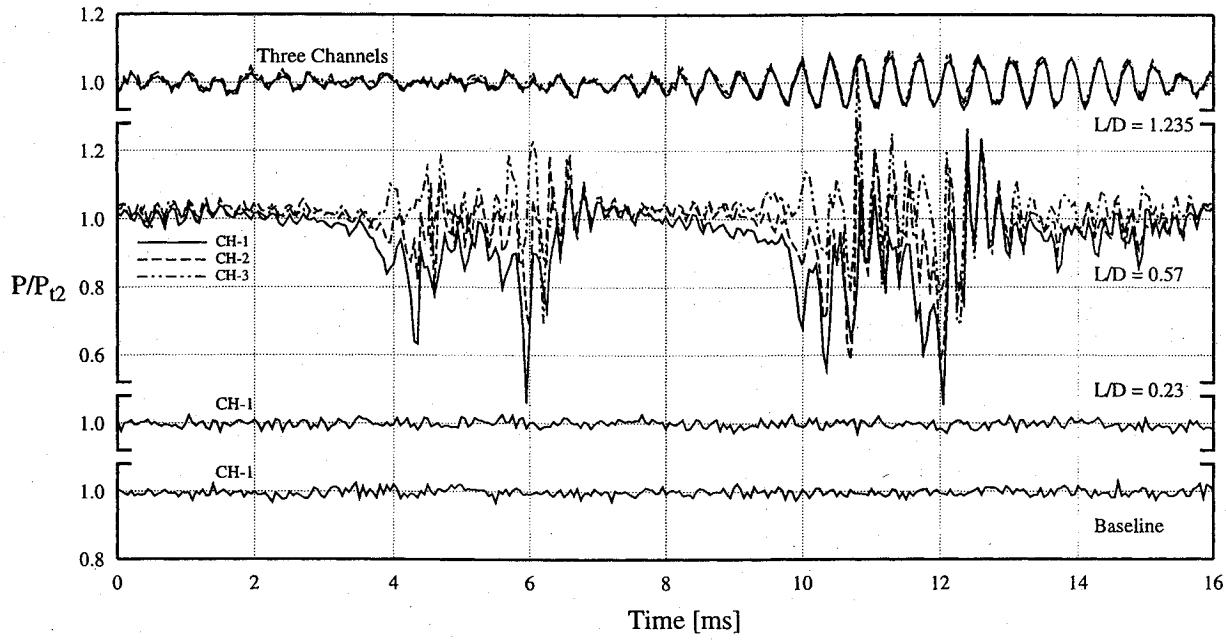

Fig. 6 Sample pressure signals at cavity base (experimental).

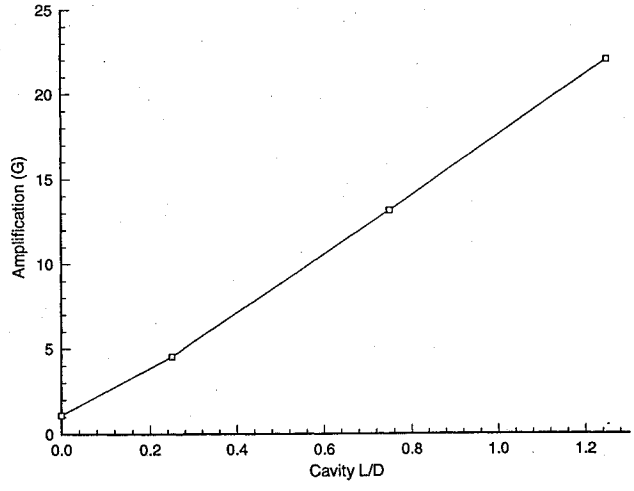

Fig. 7 Amplification vs cavity *L/D* (numerical *D* = 2.54 cm).

Figure 6 also shows pressure signals for the deep-cavity case, in which the oscillations become nearly sinusoidal cleaner. However, the signal does break down into a less sinusoidal mode at random intervals. The amplitudes for the deep cavity are noticeably larger than those for the medium-cavity low-amplitude mode.

Numerical simulations show a nearly linear increase in pressure amplification with cavity depth (see Fig. 7). In these simulations, a sinusoidal freestream inflow pressure, with a peak-to-peak amplitude of $\pm 0.02 P_\infty$, drives the pressure oscillations at the input frequency that produces the largest amplification of the cavity. This frequency is determined computationally by trial and error and is typically close to the primary frequency estimated from Eq. (2). The sensitivity of amplification to changes in frequency and input amplitude for several cavity geometries is currently under study. Finally we note that even with the strongest numerical oscillations, shock waves are not observed inside the cavity.

Pressure Oscillations vs Lip Radius

Pressure oscillations are weakly sensitive to lip geometry for the range of lip radii from 0.1 to 1.0 mm. The flow dynamics near the cavity base is not substantially affected by changes in the lip shape in the experiments, as can be seen in power spectra (see Ref. 11) for all three cavity depth ranges. There is especially weak sensitivity for the deep cavities. Numerical time-accurate runs also indicate modest sensitivity of G to small changes in lip radius. The amplification for $L/D = 0.25$ and 0.75 changes less than 5 and 20%, respectively, as the lip radius is varied.

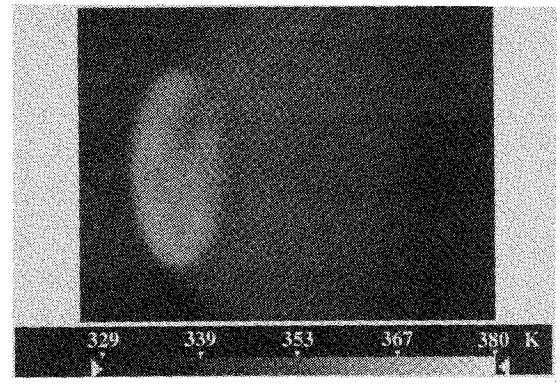

Fig. 8 IR image for *L/D* = 0.23, sharp-lip cavity.

Flowfield Structure and Surface Heating for a Shallow Cavity with a Sharp Lip

Agreement between experiment and computations is good for the flowfield structure and surface heating for the shallow, sharp-lip cavity configuration. Experimental results for a sharp lip (roughly 0.1-mm radius) and shallow cavity ($L/D = 0.25$) show a reduction in temperature in the vicinity of the cavity lip (a cool ring). As can be seen in the IR image in Fig. 8, this dark ring begins at the cavity edge and extends downstream about 6–7 deg in terms of the angle measured from the hemispherical nose center.

Numerical, steady-state results for the same configuration confirm that this cool region exists and can be attributed to the presence of a separated recirculation region. This region is small, and a fine grid (150×150, including 70 cells along the outer surface and 10^{-4}-mm surface cell thickness) is required to resolve the details. There is an inflow into the cavity along the centerline, where the pressure is greatest, and an outflow near the lip of the cavity, where the pressure is slightly lower (Fig. 9). The outflow around the sharp lip separates and forms a recirculation zone just outside the cavity lip. Where the flow reattaches, it turns slightly as it reaches the surface, creating a weak oblique shock.

Numerical results show that the recirculation zone consists of one primary vortex and one small secondary vortex within the primary vortex and near the lip (Fig. 10). The primary vortex reattaches at approximately 10 deg from the lip, along the spherical outer surface. This reattachment point corresponds to the peak heat transfer along the outer surface and to roughly the edge of the cool ring in the IR image. The secondary vortex separates at about 5 deg from the lip.

The kerosene-lampblack visualization technique has been used to obtain surface flow patterns around the cavity edge and verify

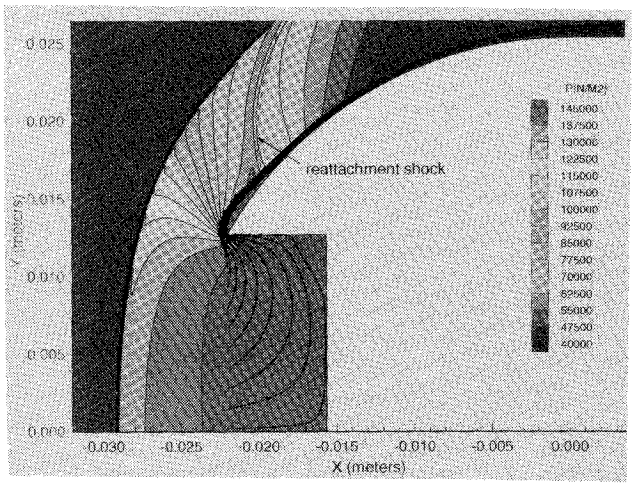

Fig. 9 Pressure contours and select streamlines (numerical; L/D = 0.25, 0.1-mm lip radius).

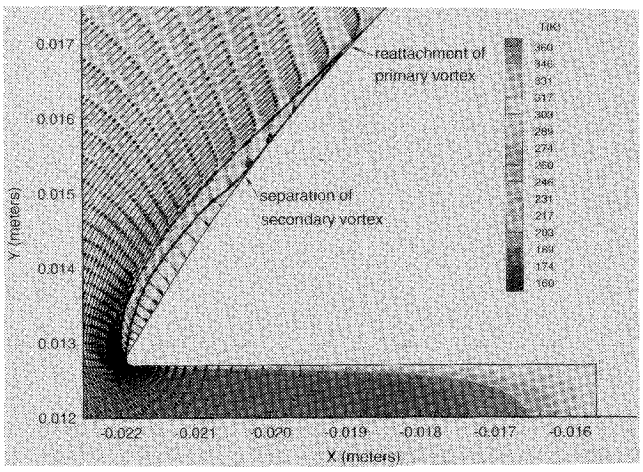

Fig. 10 Close-up of recirculation zone (numerical; L/D = 0.25, 0.1-mm lip radius).

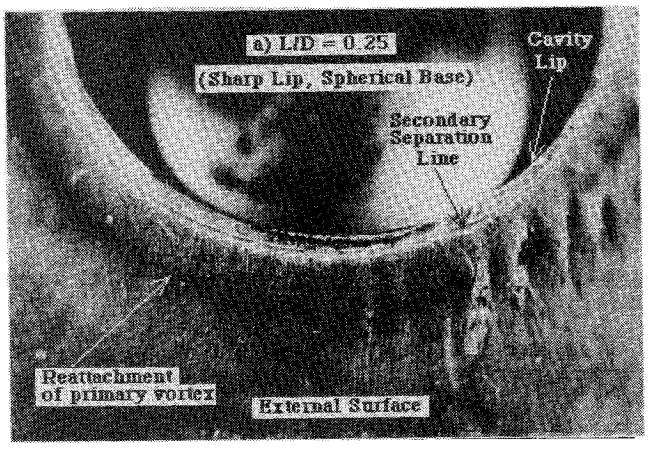

Fig. 11 Surface oil-flow photograph (L/D = 0.23, sharp lip).

the details of the recirculation zone for this configuration. Figure 11 shows a separation line (i.e., oil accumulation) near the lip, corresponding roughly to the position of the separation of the secondary vortex estimated numerically. Further downstream is the reattachment line for the primary vortex, that appears as a dark ring.

Figure 12 provides a spatially converged numerical estimate of the steady-flow heat transfer distribution along the surface. The cool ring corresponds to the region between the lip (s = 1.9 cm) and the reattachment point (s = 2.3 cm). The maximum heating (approximately 90 kW/m^2) for this cavity configuration occurs in a small region inside the cavity near the lip, where the flow is highly accelerated and the boundary layers are thin (roughly 10^{-5} m). Experimental thermal images verify that the heating just inside the lip is severe (a white ring is seen), but it has not been directly quantified. Time-accurate simulation with inflow noise indicates only minor fluctuations in the size of the recirculation region and the magnitude of surface heating (less than ±10%). We also find numerically that the thermal boundary layer is large and convection small at the base of the cavity. This accounts for the relatively low heat fluxes there.

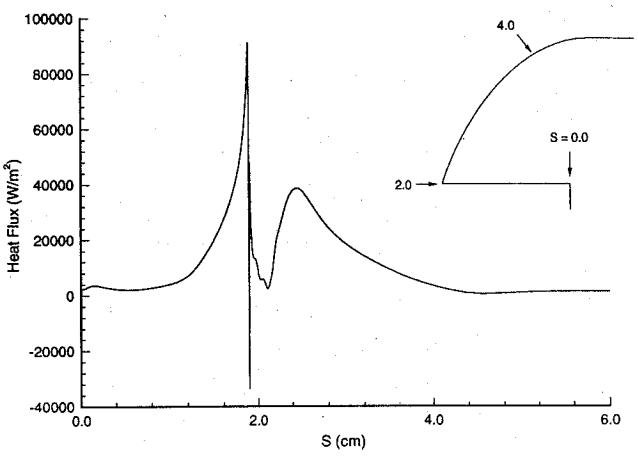

Fig. 12 Surface heat-flux distribution (numerical; L/D = 0.25, 0.1-mm lip).

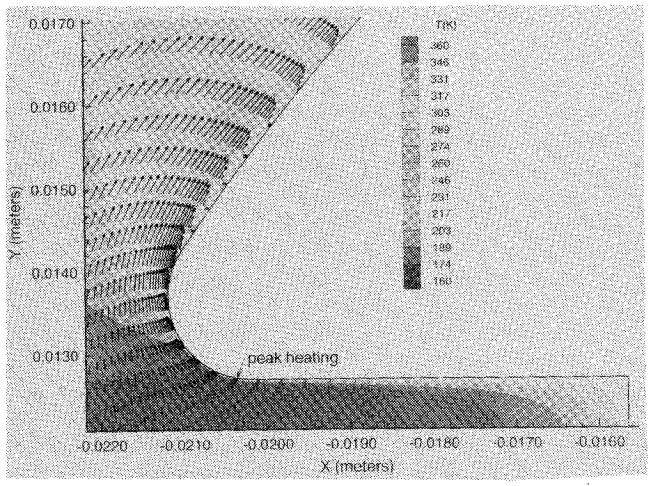

Fig. 13 Temperature contours (numerical; L/D = 0.25, 1.0-mm lip radius).

Flowfield Structure and Surface Heating vs Lip Radius

Experimental and computational results indicate that the flowfield structure and surface heating rates are sensitive to lip radius. Numerical study shows that as the lip radius is increased from 0.1 (described above) to 1.0 mm, the recirculation region becomes thinner and smaller, the secondary vortex disappears, and the reattachment shock weakens (Fig. 13). For a lip radius of 2.0 mm, the recirculation region in the numerical solution completely disappears. Experiments confirm that the cool ring disappears when the lip radius is increased from 0.1 to 1.5 mm.

We also find that peak heating is reduced as the lip radius is increased from 0.1 to 2.0 mm. Spatially converged numerical results show that by rounding the lip radius from 0.1 to 1.0 mm, the peak heating drops 44% to values comparable to the stagnation-point heating of the baseline case (Fig. 14). As the lip is rounded, the peak heating region just inside the cavity, near the lip, moves out of the cavity and along the lip. The IR camera results confirm that rounding the lip to 1.5 mm generates temperatures at the lip that are roughly the same as the stagnation-point temperature of the baseline case.

Flowfield Structure and Surface Heating vs Cavity Depth

Numerically steady solutions indicate that the flowfield structure and surface heating near the cavity lip are insensitive to cavity depth, beyond some critical depth of approximately L/D = 0.2. Beyond

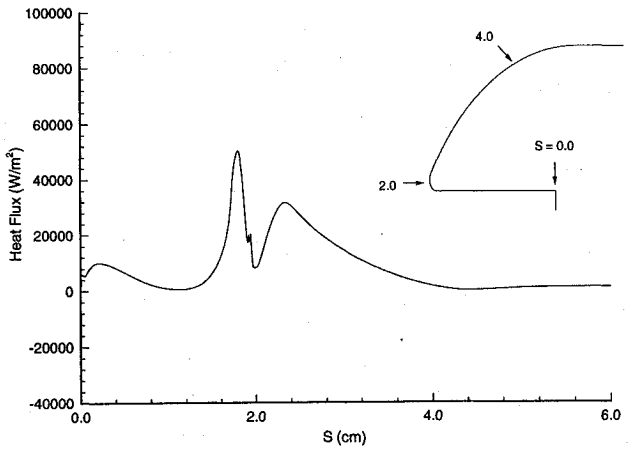

Fig. 14 Surface heat-flux distribution (numerical; $L/D = 0.25$, 1.0-mm lip).

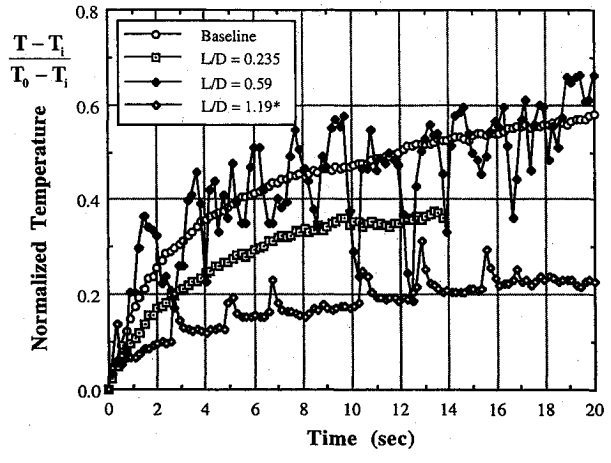

Fig. 15 Normalized temperature histories (experimental) at point 2 for sharp-lip cavities.

this depth the flow is virtually stagnant at the base of the cavity and thus has little overall effect on the flow near the cavity front. This numerical result is obtained for both sharp and blunted lips.

In the experiments the flowfield structure and surface heating are sensitive to cavity depth, except for the shallow cavities, for which the oscillations are weak. The temperature history results for medium cavities (in which the large-amplitude oscillation mode was found) demonstrate sensitivity to base shape and L/D and require further study.[11]

The experimental deep-cavity, sharp-lip case has a slightly larger cool ring than the shallow-cavity case. The strong oscillations associated with deeper cavities cause the location of reattachment to vary along the outer surface. This mechanism may account for the increased ring size. The IR images for the deep-cavity, rounded-lip case show no significant differences from the shallow-cavity, rounded-lip case (i.e., both cases show reduction or elimination of the cool ring).

Experimental surface temperature histories at point 2 (just outside the cavity lip) for the sharp-lip cases are shown in Fig. 15. The temperature histories are normalized using the stagnation temperature and the initial surface temperature. The temperatures are much lower, compared to the baseline case, for both the shallow- and deep-cavity cases, because of the recirculation region, and the deep cavity is significantly cooler than the shallow cavity. These results for the deep and medium (see Ref. 11) cavities suggest a link between strong oscillations and cooling of the lip.

Conclusion

Resonant pressure oscillations within a forward-facing cavity in hypersonic flow are an experimental flow feature but occur numerically only if freestream fluctuations are present for the cavity geometries presented ($L/D < 1.25$). The oscillations are dominated by the quarter-wave frequency of the cavity. In the numerical simulations, the oscillation strength increases with cavity depth. In the experiments, it increases with cavity depth for relatively shallow cavities ($L/D < 0.4$). For somewhat deeper cavities ($0.4 < L/D < 0.7$), experiments show that the pressure oscillations within the cavity switch randomly between two modes of behavior involving small-and large-amplitude fluctuations. The fluctuations for still deeper cavities ($0.7 < L/D < 1.25$) return to moderate levels and become nearly sinusoidal.

Agreement between experiment and computations is good for the flowfield structure and surface heating. Sharp lips produce both a recirculation region, which cools the outer surface, and severe heating just inside the cavity. Rounding the lip eliminates the recirculation region and alleviates heating inside the cavity. Numerical steady results indicate that flowfield structure and outer surface heating are insensitive to cavity depth. Experimental results hint that the strong oscillations associated with deep cavities may produce an additional cooling effect.

Acknowledgments

Funding was provided by the Institute for Advanced Technology under Armament Research, Development and Engineering Center Contract DAAA21-93-C0101, monitored by William G. Reinecke and Dennis Wilson. The authors are grateful to the Center for Energy Studies of the University of Texas at Austin for providing the IR camera system for the experiments; to NASA for use of the NAS Supercomputer Center at NASA Ames Research Center; to Cray Research, Inc., for use of the Cray Y-MP at the University of Texas at Austin; and to Scott Imlay of Amtec Engineering for providing technical assistance with the numerical simulations. The commercial finite volume code INCA and grid package GRIDALL were licensed from Amtec Engineering.

References

[1]Hohler, V., and Stilp, A. J., "Long Rod Penetration Mechanics," *High Velocity Impact Mechanics*, 1st ed., edited by Jonas A. Zukas, Wiley, New York, 1990, pp. 321–404.

[2]Baker, J., and Williams, A., "Hypervelocity Penetration of Plate Targets by Rod-Like Projectiles," *International Journal of Impact Engineering*, Vol. 5, No. 1, 1987, pp. 101–110.

[3]Hartmann, J., and Troll, B., "On a New Method for the Generation of Sound Waves," *Physical Review*, Vol. 20, pp. 719–727, 1922.

[4]Powell, A., and Smith, T. J., "Experiments Concerning the Hartmann Whistle," Dept. of Engineering, Rept. 64-42, Univ. of California at Los Angeles, CA, Sept. 1964.

[5]Burbank, P. B., and Stallings, R. L., "Heat-Transfer and Pressure Measurements on a Flat-Face Cylinder at a Mach Number Range of 2.49 to 4.44," NASA TMX-221, 1959.

[6]Huebner, L. D., and Utreja, L. R., "Experimental Flowfield Measurements of a Nose Cavity Configuration," Society of Automotive Engineers, Paper 871880, Oct. 1987.

[7]Sambamurthi, J. K., Huebner, L. D., and Utreja, L. R., "Hypersonic Flow over a Cone with Nose Cavity," AIAA Paper 87-1193, June 1987.

[8]Marquart, E. J., Grubb, J. B., and Utreja, L. R., "Bo-Shock Dynamics of a Forward-Facing Nose Cavity," AIAA Paper 87-2709, Oct. 1987.

[9]Huebner, L. D., and Utreja, L. R., "Mach 10 Bow-Shock Behavior of a Forward-Facing Nose Cavity," *Journal of Spacecraft and Rockets*, Vol. 30, No. 3, 1993, pp. 291–297.

[10]Yuceil, B., Dolling, D. A., and Wilson, D., "A Preliminary Investigation of the Helmholtz Resonator Concept for Heat Flux Reduction," AIAA Paper 93-2742, July 1993.

[11]Yuceil, B., and Dolling, D. S., "Effects of a Nose Cavity on Heat Transfer and Flowfield over a Blunt Body at Mach 5," AIAA Paper 94-2050, June 1994.

[12]Imlay, S. T., Roberts, D. W., and Soetrisno, M., "HANA—A Three-Dimensional Navier–Stokes Code for Chemically Reacting Flows," AIAA Paper 91-2153, June 1991.

[13]Steger, J. L., and Warming, R. F., "Flux Vector Splitting of the Inviscid Gasdynamic Equations with Applications to Finite-Difference Methods," *Journal of Computational Physics*, Vol. 40, No. 2, 1981, pp. 263–293.

[14]Fay, J. A., and Riddell, F. R., "Theory of Stagnation Point Heat Transfer in Dissociated Air," *Journal of the Aeronautical Sciences*, Vol. 25, No. 2, 1958, pp. 73–97.

T. C. Lin
Associate Editor